

Triggering Collapse of the Presolar Dense Cloud Core and Injecting Short-Lived Radioisotopes with a Shock Wave. II. Varied Shock Wave and Cloud Core Parameters

Alan P. Boss and Sandra A. Keiser

*Department of Terrestrial Magnetism, Carnegie Institution, 5241 Broad Branch Road, NW,
Washington, DC 20015-1305*

boss@dtm.ciw.edu, keiser@dtm.ciw.edu

ABSTRACT

A variety of stellar sources have been proposed for the origin of the short-lived radioisotopes that existed at the time of the formation of the earliest Solar System solids, including Type II supernovae, AGB and super-AGB stars, and Wolf-Rayet star winds. Our previous adaptive mesh hydrodynamics models with the FLASH2.5 code have shown which combinations of shock wave parameters are able to simultaneously trigger the gravitational collapse of a target dense cloud core and inject significant amounts of shock wave gas and dust, showing that thin supernova shocks may be uniquely suited for the task. However, recent meteoritical studies have weakened the case for a direct supernova injection to the presolar cloud, motivating us to re-examine a wider range of shock wave and cloud core parameters, including rotation, in order to better estimate the injection efficiencies for a variety of stellar sources. We find that supernova shocks remain as the most promising stellar source, though planetary nebulae resulting from AGB star evolution cannot be conclusively ruled out. Wolf-Rayet star winds, however, are likely to lead to cloud core shredding, rather than to collapse. Injection efficiencies can be increased when the cloud is rotating about an axis aligned with the direction of the shock wave, by as much as a factor of ~ 10 . The amount of gas and dust accreted from the post-shock wind can exceed that injected from the shock wave, with implications for the isotopic abundances expected for a supernova source.

Subject headings: hydrodynamics – instabilities – solar system: formation – stars: formation

1. Introduction

The origin of the short-lived radioisotopes (SLRIs) that were present during the formation of the earliest solids in the protoplanetary disk that formed our planetary system remains as a largely unsolved mystery (Dauphas & Chaussidon 2011; Boss 2012). SLRIs such as ^{60}Fe and ^{26}Al , with half-lives of 2.62 Myr and 0.717 Myr, respectively, have been ascribed to nucleosynthesis in Type II (core collapse) supernovae, asymptotic giant branch (AGB) stars, or, for ^{26}Al , in addition to these stellar nucleosynthetic sources, to irradiation of the inner edge of the solar nebula by the protosun. Having a nearby supernova as a source of SLRIs requires that the Sun formed in a massive cluster with at least 1000 stars, so that at least one of the stars is likely to have a mass greater than $25 M_{\odot}$ (e.g., Dukes & Krumholz 2012). Most stars are born in such clusters, making such a birth site a likely possibility for the Sun. Intermediate-mass ($\sim 5 M_{\odot}$) AGB stars are possible sources for these SLRIs (Huss et al. 2009). Super-AGB stars, with masses in the range of 7 to $11 M_{\odot}$, are also possible sites for synthesizing the SLRIs ^{60}Fe and ^{26}Al , as well as ^{41}Ca , with a half-life of 0.102 Myr (Lugaro et al. 2012). Due to their age, however, AGB stars are unlikely to be found in regions of ongoing star formation: Kastner & Myers (1994) estimated the chance that a mass-losing AGB star would pass through a molecular cloud within 1 kpc of the Sun in the next million years was only $\sim 1\%$. However, they also estimated that over a molecular cloud lifetime, the chances of an AGB star interaction could be as high as $\sim 70\%$.

Boss et al. (2010) studied the two-dimensional (2D) interactions of shock waves with a variety of speeds with a $\sim 2M_{\odot}$ cloud core, finding that shock speeds in the range of $\sim 5 \text{ km s}^{-1}$ to $\sim 70 \text{ km s}^{-1}$ were able to simultaneously trigger cloud collapse and inject significant amounts of shock wave gas and dust. Boss & Keiser (2010) showed that the injection efficiency depended sensitively on the assumed shock width and density, and suggested that thin supernova shocks were therefore preferable to the thick planetary nebula winds outflowing from AGB stars. Gritschneider et al. (2012) modeled the 2D interaction of higher speed (97.5 or 276 km s^{-1}) supernova shock waves with a $10 M_{\odot}$ cloud core, finding that simultaneous triggered collapse and SLRI enrichment was still possible in that case. Boss & Keiser (2012) extended their 2010 models to three dimensions (3D), revealing the 3D structure of the Rayleigh-Taylor (R-T) fingers that form during the shock-cloud collision and which constitute the injection mechanism.

Other injection scenarios have been investigated as well. Ouellette et al. (2007, 2010) studied the 2D injection of SLRIs from a supernova into a nearby, previously-formed protoplanetary disk, showing that injection of shock wave gas could not occur, but that refractory grains with sizes of $\sim 1\mu\text{m}$ or larger could be injected. Pan et al. (2012) studied the 3D interaction of a supernova remnant with the gaseous edge of the HII region created by a

supernova’s progenitor star, finding that the supernova ejecta could contaminate enough of the molecular cloud gas to explain the observed levels of some Solar System SLRIs.

Recent research has cast significant doubt on the initial amount of ^{60}Fe in the solar nebula. The initial ratio $^{60}\text{Fe}/^{56}\text{Fe}$ was once thought to be high enough to require a nearby supernova. However, new whole rock analyses on a range of meteorites have lowered this initial ratio to an apparently Solar-System-wide, uniform ratio of 1.15×10^{-8} (Tang & Dauphas 2012). Other studies have also found significantly lower ratios (3×10^{-9} : Moynier et al. 2011), or cast severe doubt on the much higher ratios previously found (Telus et al. 2012). Given that the interstellar medium (ISM) has a $^{60}\text{Fe}/^{56}\text{Fe}$ ratio of $\sim 2.8 \times 10^{-7}$, Tang & Dauphas (2012) suggest that the meteoritical ^{60}Fe may have originated from the ISM rather than a nearby supernova, though this would require the presolar cloud to have formed from a molecular cloud that had not been injected with any fresh ^{60}Fe for ~ 15 Myr, allowing the ^{60}Fe to decay for ~ 5 half-lives, reducing the ISM $^{60}\text{Fe}/^{56}\text{Fe}$ ratio by a factor of ~ 30 to the meteoritical value. Tang & Dauphas (2012) then suggest that the solar nebula’s ^{26}Al may have arisen from the ^{26}Al -rich, ^{60}Fe -poor wind of a pre-supernova massive ($> 30M_{\odot}$) star, i.e., a Wolf-Rayet (WR) star (e.g., Gaidos et al. 2009; Tatischeff et al. 2010). Tang & Dauphas (2012) predict that if their suggestion is correct, calcium, aluminum-rich inclusions (CAIs), which have some variability in their initial $^{26}\text{Al}/^{27}\text{Al}$ ratios (e.g., Krot et al. 2012), should have uniform initial $^{60}\text{Fe}/^{56}\text{Fe}$ ratios.

Gounelle and Meynet (2012) also proposed that the SLRIs came from a mixture of supernovae (for the ^{60}Fe) and massive star winds (for the ^{26}Al) from several generations of stars in a giant molecular cloud (GMC). Their scenario proposes that a first generation of massive stars became supernovae and ejected ^{60}Fe and ^{26}Al into the GMC. After 10 Myr, a second generation of massive O stars formed, with the wind from one of them sweeping up GMC gas into an expanding shell of gas rich with ^{26}Al from its own outflow. Because of the shorter half-life of ^{26}Al compared to ^{60}Fe , after 10 Myr the ^{60}Fe from the first generation of massive stars has decayed much less than the original ^{26}Al , which has essentially disappeared. Gounelle and Meynet (2012) then propose that the Sun formed from the expanding shell surrounding the massive star’s HII region, before the massive star itself becomes a supernova. It is unclear, however, whether a single GMC, with a typical mass of $\sim 10^6 M_{\odot}$, could have two distinct episodes of massive star formation, separated by 10 Myr, with no other massive star formation occurring during this interval.

Tang & Dauphas (2012) point out another possible explanation for low $^{60}\text{Fe}/^{56}\text{Fe}$ ratios and high $^{26}\text{Al}/^{27}\text{Al}$ ratios: ^{26}Al is synthesized in the outer layers of massive stars, whereas ^{60}Fe is formed in the inner layers. If only the outer layers of the progenitor star are ejected during the supernova explosion, or if only the outer layers of the supernova shock are injected into

the presolar cloud, then the proper mixture of SLRIs might result from a nearby supernova (e.g., Gritschneider et al. 2012). Boss & Foster (1998), however, found that the tail-end gas in a shock front can be injected into a cloud core as efficiently as the leading-edge gas, casting some doubt on this explanation.

Recent measurements of $^{41}\text{Ca}/^{40}\text{Ca}$ ratios in CAIs (Liu et al. 2012) have lowered the previously determined meteoritical ratio of $(1.41 \pm 0.14) \times 10^{-8}$ to a value of $\sim 4.2 \times 10^{-9}$, about 10 times less than expected ISM ratios, which lie in the range of $\sim 1.6 \times 10^{-8}$ to $\sim 6.4 \times 10^{-8}$ based on steady state galactic nucleosynthesis models. This finding implies that the Solar System’s ^{41}Ca may have decayed in, e.g., a GMC, for about 0.2 to 0.4 Myr prior to CAI formation (Liu et al. 2012), much shorter than the inferred free decay interval for ^{60}Fe noted above. Alternatively, the ^{41}Ca may have been injected into the presolar cloud or solar nebula shortly before CAI formation (Liu et al. 2012).

Given the latest results on the Solar System’s $^{60}\text{Fe}/^{56}\text{Fe}$ and $^{41}\text{Ca}/^{40}\text{Ca}$ ratios, it behooves us to reinvestigate the injection efficiencies of a wide variety of possible shock waves, ranging from massive star winds, to planetary nebulae, to classic supernovae shock waves, and to also reconsider how injection efficiencies might depend on the location of SLRIs in the incoming shock wave. In this paper we explore the effects of a wider range of shock wave and cloud core properties than we have previously considered, including shock speed, thickness, density, and temperature, and cloud core mass and rotation. We restrict our exploration to 2D models, in order to more rapidly explore the large parameter space of interest.

2. Numerical Methods and Initial Conditions

The numerical calculations were performed with the FLASH2.5 adaptive mesh refinement (AMR) code (Fryxell et al. 2000). The numerical methods and initial conditions are very much the same as those used and described by the previous papers in this series (Boss et al. 2008, 2010; Boss & Keiser 2010, 2012), and so will not be repeated here. Only a brief synopsis of the key details from Boss et al. (2008, 2010) will be given here, for completeness.

As in Boss et al. (2008, 2010), we used the axisymmetric, 2D cylindrical coordinate (R , Z) version of FLASH2.5. For the standard models, the grid was 0.2 pc long in Z (the direction of shock wave propagation) and 0.065 pc wide in R . The initial number of grid blocks was 5 in R and 15 in Z , with each 2D block consisting of $8^2 = 64$ grid points; the maximum number of levels of grid refinement permitted was 5. Outflow boundary conditions were used at all surfaces of the cylinder. Self-gravity was calculated using the multipole expansion method, using Legendre polynomials up to and including $l = 10$.

The standard target clouds were Bonnor-Ebert spheres of molecular hydrogen gas with initial central densities of $1.24 \times 10^{-18} \text{ g cm}^{-3}$, radii of 0.058 pc, and masses of $2.2 M_{\odot}$, centered at $R = 0$ and $Z = 0.13$ pc. Bonnor-Ebert-like density profiles have been inferred for dense molecular cloud cores, such as Barnard 68 (Burkert & Alves 2009) and L1696A (Ruoskanen et al. 2011). In the Perseus molecular cloud, starless cores appear to have radial density profiles that are shallower than that of the singular isothermal sphere, where $\rho \propto r^{-2}$ (Schnee et al. 2010), and hence are roughly consistent with a Bonnor-Ebert-like initial profile.

The standard initial shock had a shock gas density $\rho_s = 3.6 \times 10^{-20} \text{ g cm}^{-3}$ and shock width $w_s = 9.3 \times 10^{15} \text{ cm} = 0.0030 \text{ pc}$. The mass of the shock that was incident upon the target cloud was $0.017 M_{\odot}$. The post-shock wind had a density of $3.6 \times 10^{-22} \text{ g cm}^{-3}$. Both the standard shock gas and the post-shock wind gas had initial temperatures of 1000 K, while the target cloud and its ambient medium started at 10 K, the latter with the same density as the post-shock wind. Compressional heating and radiative cooling were included, using the results of Neufeld & Kaufman (1993) for cooling caused by optically thin molecular gas composed of H_2O , CO , and H_2 . A color field was defined to be non-zero initially in the shock front, in order to be able to trace the degree to which shock front gas and dust were injected into the collapsing protostellar cloud. In several models, separate color fields were also initialized for the post-shock wind and the pre-shock, ambient medium, to learn the fate of this material as well.

3. Results

We present the results for a large range of variations in the assumed parameters for the shock front and the target cloud. In each case, we wish to compare the results for shock wave injection efficiencies to those obtained with a standard model. Hence we begin with a summary of the results for the three standard models.

3.1. Standard Models

Table 1 summarizes the three standard models (v10, v40, and v70), which are identical to the standard cloud and shock described above, differing only in the assumed shock speeds: 10, 40, and 70 km s^{-1} , respectively. These models are similar to those presented by Boss et al. (2010), except that the present models are for target clouds with twice the mass of the Boss et al. (2010) clouds. Boss et al. (2010) found that shock speeds in the range of 5–70 km

s^{-1} were able to simultaneously trigger collapse and inject significant shock wave material: slower shocks were unable to trigger collapse, while faster shocks shredded the target clouds. Hence we focus here on the same range of shock speeds.

Figure 1 depicts the evolution of model v40, which is typical in all respects of the models where simultaneous triggered collapse and injection occurs. The initial shock wave, moving at 40 km s^{-1} , strikes and compresses the edge of the target cloud, generating Rayleigh-Taylor fingers, leading to the onset of dynamic collapse along the symmetry axis ($R = x = 0$) and the formation of a protostar within $\sim 10^5 \text{ yr}$. Figure 1 shows that the protostar is accelerated by the shock front to a speed of $\sim 1 \text{ km s}^{-1}$. While significant, such speeds are small with respect to the typical velocity dispersions seen for T Tauri stars in Taurus and Orion, where dispersions of ~ 5 to 10 km s^{-1} are observed (Walter et al. 2000).

Figure 2 shows the extent to which gas and dust from the shock wave, the post-shock wind, and the ambient medium, are injected into the collapsing protostar seen in Figure 1d. The velocity vectors show that while most of this gas is blown downwind by the shock and post-shock wind, some fraction of this material will be accreted by the protostar.

Boss & Keiser (2012) discussed several of the reasons why estimates of the injection efficiency are difficult to determine. Here we follow Boss & Keiser (2012), and define the injection efficiency f_i to be the fraction of the incident shock wave material that is injected into the collapsing cloud core. Table 1 then summarizes the amount of mass derived from the shock wave, post-shock wind, and the ambient medium that is injected into the densest region of the collapsing protostar, i.e., regions with density greater than $10^{-16} \text{ g cm}^{-3}$, as used by Boss & Keiser (2012). Table 1 shows that the injection efficiencies for shock wave material are of order $f_i \sim 10^{-2}$ for the standard models, as found by Boss & Keiser (2010, 2012). In addition, the amount of injected gas derived from the post-shock wind is typically 10 times higher, while that derived from the ambient medium (i.e., the pre-shock gas) is typically over 10 times lower.

3.2. Varied Target Cloud Densities and Radii

We first consider variations on standard model v40, where the density and radius of the target cloud are changed. Figure 3 shows the result for a cloud that was shredded by a 40 km s^{-1} shock and failed to collapse – model v40-m1.9-r2, with a target cloud density 10 times lower than for model v40 (initial central density of $1.24 \times 10^{-19} \text{ g cm}^{-3}$) and a cloud radius twice as large (0.116 pc), leading to an initial cloud mass of $1.9 M_\odot$. Given that the shock in this model was identical to that in model v40 (Figures 1 and 2), it is clear that

certain shock waves will only trigger the collapse of suitably dense initial cloud cores. In fact, the same result – a shredded cloud without sustained collapse – was obtained when the initial central density was decreased by only a factor of 5 to $2.48 \times 10^{-19} \text{ g cm}^{-3}$ along with the doubled cloud radius, for a cloud mass of $3.7 M_{\odot}$. Shredding continued for these clouds when the shock width was reduced by a factor of 10 to $w_s = 0.0003 \text{ pc}$ and the standard shock gas density ($\rho_s = 3.6 \times 10^{-20} \text{ g cm}^{-3}$) was increased by factors of 10, 100, 200, 300, 400, and 1000. All of these models refused to collapse, even when the computational volume was expanded to 20 blocks in $Z = y$, the direction of shock wave propagation, to allow more time for collapse to begin before the cloud disappears off the lower edge of the AMR grid.

However, when the initial central density was decreased by a factor of 3.33 to $3.72 \times 10^{-19} \text{ g cm}^{-3}$, along with the doubled cloud radius, raising the initial cloud mass to $5.4 M_{\odot}$, dynamic collapse was achieved for the standard 40 km s^{-1} shock (model v40-m5.4-r2). Table 2 summarizes the injection efficiencies achieved for several of these models with varied shock densities and widths, all with the number of blocks in the $R = x$ direction doubled to 10. It can be seen that the values of f_i are typically $\sim 10^{-4}$ to $\sim 10^{-3}$ for these $5.4 M_{\odot}$ cloud models; however, $f_i = 0$ for model v40-m5.4-r2-w0.1-s400, as this model was compressed to a maximum density of $\sim 10^{-16} \text{ g cm}^{-3}$, but was not quite driven into sustained collapse.

3.3. Varied Target Cloud Rotation Rates

Table 3 summarizes the models with variations in the initial angular velocity (Ω_i , in rad s^{-1}) about the $Z = y$ axis. All models had the standard shock with $v_s = 40 \text{ km s}^{-1}$ and the standard $2.2 M_{\odot}$ target cloud, differing only in the initial rate of solid body rotation. The initial rotation rates of $10^{-16} \text{ rad s}^{-1}$ to $10^{-12} \text{ rad s}^{-1}$ span the range from essentially no rotation to the most rapid rotation rate possible for collapse to occur for an isolated dense cloud core. Typical observed rotation rates for dense cloud cores span the range of $\sim 10^{-14} \text{ rad s}^{-1}$ to $\sim 10^{-13} \text{ rad s}^{-1}$ (Goodman et al. 1993).

The rotation axis is the same as the symmetry axis, as that is the only possible configuration allowed for 2D, axisymmetric clouds. The effect of rotation will then be to flatten a collapsing cloud into the direction perpendicular to the rotation axis (i.e., outward along the $x = R$ axis), forming a rotationally flattened, protostellar disk that will be smacked face-on by the shock front. Such a configuration should lead to enhanced injection efficiencies by the target cloud. Table 3 shows that, compared to the standard, non-rotating model v40, when cloud rotation is included, significantly higher injection efficiencies are obtained, as expected, by as much as a factor of ~ 10 . Figure 4 shows the results for four models with increasingly higher values of Ω_i : as Ω_i increases, the collapsing protostar is accompanied by

a progressively larger region with relatively high gas density (yellow-green regions), compared to the non-rotating model v40 (Figure 2a), allowing more shock wave material to be intercepted in cloud gas that is likely to be accreted. Model v40-o13, in fact, can be seen to have formed a structure similar to a large scale (~ 1000 AU) protostellar disk (Figure 4c). However, when Ω_i is increased to 10^{-12} rad s $^{-1}$, as in model v40-o12, the cloud does not collapse, and instead is shredded by the shock wave. Hence the extent to which initial cloud rotation can enhance the injection efficiency is limited in the end by the desire to also achieve high enough densities for dynamic collapse to ensue. In addition, shock fronts which strike clouds where the rotation axis is not aligned with the direction of shock propagation will not be able to inject quite as much shock front matter, lowering the injection efficiencies. The present results for aligned rotation axes and shock propagation directions thus represent upper bounds for the possible enhancements due to rotation. A fully 3D study will be needed to learn about injection efficiencies in the case of non-aligned rotation axes.

3.4. Varied Target Cloud Density Distribution

Table 4 summarizes the models with variations in the initial target cloud density distribution, namely a perturbation to the Bonnor-Ebert sphere with a binary perturbation along the symmetry ($Z = y$) axis, as seen in Figure 5a. These models have a reference density of 4.1×10^{-19} g cm $^{-3}$, three times lower than the standard target clouds, yielding an initial cloud mass of $1.0 M_\odot$. These clouds are so low in mass, in fact, that when evolved without any shock wave, they expand and do not collapse. Hence these clouds represent clumpy regions of the ISM that would not collapse on their own, in contrast to the other, more massive target clouds, which eventually collapse on their own, even without being struck by a shock wave.

Figure 5 shows that in spite of this basic difference, when struck by a suitable shock wave, the $1.0 M_\odot$ clouds can still be driven into sustained gravitational collapse, in much the same way as the other models. However, when v_s is increased to 20 km s $^{-1}$ or above, these low density clouds are shredded and do not collapse. Table 4 summarizes these results, and shows that for the shock speeds that do lead to collapse, the injection efficiencies can be significant, i.e., f_i as high as 5.2×10^{-2} for model v10-m1.0.

3.5. Varied Shock and Post-Shock Wind Temperatures

Table 5 summarizes the models with variations in the maximum shock (T_s) and post-shock wind (T_{ps}) temperatures, compared to a standard shock model with $T_s = T_{ps} = 1000$ K. All models collapse, except for model v40-T100-s100, where the shock density was too high to result in collapse, given the other parameters. The injection efficiencies varied from 2.7×10^{-4} to 1.8×10^{-2} for the $T_s = T_{ps} = 100$ K models, differing only in the value of ρ_s . These models demonstrate that injection efficiencies continue to be significant, even for considerably cooler shock and post-shock temperatures than the standard values.

3.6. Varied Shock Speeds, Densities, and Widths

Tables 6, 7, and 8 present the results for variations in the shock densities (ρ_s) and widths (w_s), for shock speeds (v_s) of 10, 40, and 70 km s⁻¹, respectively. Many of these models had extended grids ($N_y = 30$ or 40) in the shock direction ($Z = y$) in order to allow the cloud to be followed downstream far enough to determine if collapse would ensue. The models with $M_s = 0$ were models where collapse did not occur.

Table 6 lists the models with $v_s = 20$ km s⁻¹, showing that with a wide variety of shock densities and widths, injection efficiencies of $\sim 10^{-2}$ to $\sim 10^{-1}$ can result if collapse occurs. All of the 40 km s⁻¹ models listed in Table 7 were also described in Boss & Keiser (2010), but with the difference here that an improved methodology for estimating the injection efficiencies (Boss & Keiser 2012) is used here, which usually results in higher estimates of f_i . Both estimates are listed in Table 7 for ease of comparison. Finally, Table 8 shows that for 70 km s⁻¹ shocks, injection efficiencies are still significant, with $f_i \sim 10^{-3}$ to $\sim 10^{-2}$, but are typically lower; e.g., $f_i = 7.4 \times 10^{-2}$, 5.0×10^{-2} , and 8.6×10^{-3} for models v10-w0.1, v40-w0.1, and v70-w0.1, respectively.

3.7. Discussion

We now turn to a discussion of which models might be the most appropriate representations of observed stellar outflows and shock waves that might be carriers of freshly-synthesized SLRIs. Supernovae resulting from the core collapse of massive stars in the range of $\sim 20 - 60M_\odot$ and planetary nebulae derived from intermediate-mass ($\sim 5M_\odot$) AGB (Huss et al. 2009) or higher mass ($\sim 7 - 11M_\odot$) super-AGB stars (Lugaro et al. 2012) have been proposed as possible sources of many Solar System SLRIs. In addition, significant amounts of ²⁶Al are contained in the outflows of massive Wolf-Rayet stars, which are the predecessors

to many Type II SN (Tatischeff, Duprat, & de Séréville 2010). ^{26}Al is abundant in the ISM: Diehl et al. (2010) detected γ -rays from the Sco-Cen association that implied the presence of $\sim 1.1 \times 10^{-4} M_{\odot}$ of live ^{26}Al . If this amount of ^{26}Al pollutes a $\sim 10^6 M_{\odot}$ GMC containing ^{27}Al at Solar System abundances (Anders & Grevesse 1989), then the GMC would have a ratio $^{26}\text{Al}/^{27}\text{Al} \sim 3 \times 10^{-6}$, well below the inferred initial Solar System canonical level of $^{26}\text{Al}/^{27}\text{Al} \sim 5 \times 10^{-5}$ (MacPherson et al. 2012).

The Cygnus Loop is a $\sim 10^4$ yr-old core collapse (Type II) supernova remnant (SNR) with $v_s \approx 170$ km/sec and $w_s < 10^{15}$ cm (Blair et al. 1999), a width consistent with our thin shock models, with $0.1w_s = 9.3 \times 10^{14}$ cm. W44 is also a core collapse SNR with $v_s = 20 - 30$ km/sec and a width less than 10^{16} cm (Reach et al. 2005), comparable to our standard shock width $w_s = 9.3 \times 10^{15}$ cm. Hence SNR appear to be most consistent with our models with relatively high speed (70 km s^{-1}) shocks and $0.1w_s$ or with models with lower speed ($10 - 40 \text{ km s}^{-1}$) shocks and 1 or $0.1 w_s$, respectively.

The W44 SNR is expanding into gas with a number density $n \sim 10^2 \text{ cm}^{-3}$ (Reach et al. 2005). Boss & Keiser (2012) presented results for a 3D version of our 2D model v40-w0.1-s400-20 (Table 7), a model with $v_s = 40 \text{ km s}^{-1}$, shock number density $n_s \approx 4 \times 10^6 \text{ cm}^{-3}$, and a shock width of $\approx 10^{15}$ cm. Boss & Keiser (2012) noted that the shock density n_s for an isothermal shock propagating in an ambient gas of density n_{am} is $n_s/n_{am} = (v_s/c_{am})^2$, where c_{am} is the ambient gas sound speed. For model v40-w0.1-s400-20, with $c_{am} = 0.2 \text{ km s}^{-1}$ and $n_{am} = 10^2 \text{ cm}^{-3}$, as in the case of the W44 SNR, the shock density should be $n_s = 4 \times 10^6 \text{ cm}^{-3}$, the same as the density in model v40-w0.1-s400-20. Hence shock densities about 400 times higher than in the standard shock model appear to be similar to what is expected to be the case in realistic SNRs (Boss & Keiser 2012).

During the transition from an AGB star to a post-AGB star, low mass stars generate outflows known as planetary nebulae (van Marle & Keppens 2012), with speeds of order 20 km s^{-1} . The planetary nebula Abell 39 is estimated to have a thickness of $\sim 3 \times 10^{17}$ cm (Jacoby, Ferland, & Korista 2001), while planetary nebula PFP-1 is estimated to have a thickness of $\sim 5 \times 10^{17}$ cm (Pierce et al. 2004). These thicknesses are considerably larger than the standard shock width $w_s = 9.3 \times 10^{15}$ cm, but are only a few times thicker than the models with $10w_s = 9.3 \times 10^{16}$ cm. Hence planetary nebulae appear to be most consistent with our models with low speed ($\sim 10 \text{ km s}^{-1}$) shocks and large ($10w_s$) shock widths.

3D models of the interaction of a WR fast wind (initially moving at $2 \times 10^3 \text{ km s}^{-1}$) with a previously emitted red supergiant wind (moving at $10 - 15 \text{ km s}^{-1}$) led to the formation of R-T fingers and expansion velocities of the interacting region less than 100 km s^{-1} (van Marle & Keppen 2012). The thickness of the shocked region was typically $\sim 10^{17}$ cm and the density was $\sim 4 \times 10^{-22} \text{ g cm}^{-3}$. These quantities correspond to shock widths and

densities of $\sim 10 w_s$ and $0.01 \rho_s$, respectively. The latter value is considerably lower than any of the values explored in the present study. Foster & Boss (1996) found that such a low-density shock would not have enough momentum to compress a target cloud into collapse. Furthermore, the gas temperature was forced to remain above 10^4 K everywhere in the van Marle & Keppen (2012) simulations. WR winds are fully ionized and are driven by thermal pressure. For these reasons a direct comparison to the present models is not possible. It is unclear what would happen when a WR wind shell encounters a dense molecular cloud core, but the fact that the gas is fully ionized and unable to cool below 10^4 K implies that such a hot shock would shred a target cloud to pieces (Foster & Boss 1996).

The dilution factor D is defined as the ratio of the amount of mass injected into the collapsing cloud that was derived from the shock wave (M_s) to the amount of mass derived from the target cloud. The Tables list M_s for each of the models. For a final system mass of $1 M_\odot$, the dilution factor is then simply $D = M_s/M_\odot$. However, because a supernova shock starting at ~ 2000 km s $^{-1}$ must be slowed down by snowplowing a large amount of the ISM to reach a speed as low as in these models, we follow Boss & Keiser (2012) in defining a third parameter, β , to be the ratio of shock front mass originating in the supernova to the total mass in the shock, including that swept up from the intervening ISM. In this case, the dilution factor becomes $D = \beta M_s$. For a SNR to slow down from 2000 km s $^{-1}$ to $10 - 70$ km s $^{-1}$, as in our models, $\beta = 0.005 - 0.035$. This means that the shock front must sweep up between ~ 30 and ~ 200 times its own mass before slowing to the proper speeds. In the case of the W44 SNR, moving at $20 - 30$ km/sec, the shock must have already swept up about 100 times its original mass. For a W44-like shock with $n_s = 4 \times 10^6$ cm $^{-3}$ and $w_s = 10^{15}$ cm, this means that the amount of swept-up intervening gas was $\sim 99\%$ of the shock's current gas mass, i.e., a column depth (by number) of $\sim 4 \times 10^{21}$ cm $^{-2}$. For the gas that W44 is currently expanding into, with a number density $\sim 10^2$ cm $^{-3}$ (Reach et al. 2005), this would require passing through ~ 10 pc of such intervening gas. The diameter of the W44 SNR is ~ 11 pc (Reach et al. 2005), in agreement with this estimate. Such number densities ($\sim 10^2$ cm $^{-3}$) are typical of the average giant molecular cloud densities (Williams et al. 2000).

The dilution factors needed to match inferred meteoritical abundances of SLRIs are uncertain, in part because the inferred initial abundances for some SLRIs are in flux (e.g., for ^{60}Fe , as previously noted), but also because estimates of the production rates of SLRIs such as ^{60}Fe and ^{26}Al are uncertain by large factors (Tur et al. 2010), as noted by Boss & Keiser (2012). Given these caveats, dilution factors for a supernova source range from $D \sim 10^{-4}$ to 10^{-3} (Takigawa et al. 2008) to $D = 3 \times 10^{-3}$ (Gaidos et al. 2009). Given the β factor, this means that a SN source requires models with: $1 w_s$ and 10 km s $^{-1}$ ($\beta = 0.005$) to have $M_s = 0.02 - 0.6 M_\odot$; $0.1 w_s$ and 40 km s $^{-1}$ ($\beta = 0.02$) to have $M_s = 0.005 - 0.15 M_\odot$; or $0.1 w_s$ and 70 km s $^{-1}$ ($\beta = 0.035$) to have $M_s = 0.003 - 0.09 M_\odot$; in order to cover the

range of $D \sim 10^{-4} - 3 \times 10^{-3}$. High shock densities are also indicated for a SN source. The Tables show that while none of the v10-series or v70-series models meet these requirements, two models in Table 7 (v40-w0.1-s100 and v40-w0.1-s200) reach $M_s = 0.0025$ and $0.0039 M_\odot$, respectively, close to the minimum amount needed. Given that rotation (Table 3) can increase the injection efficiencies by factors as large as 10, it appears likely that a rotating target cloud may be able to meet the required dilution factor for a $v_s = 40 \text{ km s}^{-1}$ shock.

For an AGB star, Trigo-Rodríguez et al. (2009) estimate $D \sim 3 \times 10^{-3}$. Since $\beta \sim 1$ for an AGB source, $D = M_s/M_\odot$, and an AGB source would require a model with $M_s \sim 3 \times 10^{-3} M_\odot$, $10 w_s$, and $v_s \sim 20 \text{ km s}^{-1}$. The models with $v_s = 10$ or 40 km s^{-1} come the closest to the correct shock speed. Table 6 shows that none of the v10-w10-series succeeded in triggering collapse. Table 7 shows that one of the v40-w10 series of models, v40-w10, was able to trigger collapse and inject $M_s \sim 4 \times 10^{-4} M_\odot$, about a factor of 10 times too low to support the AGB star scenario. However, the rotating target cloud models (Table 3) show that with significant rotation, M_s can be increased by a factor of 10, so in that case an AGB star remains as a possibility.

The Table 3 models show that target cloud rotation is likely to be a key factor for achieving the dilution factors apparently required for the Solar System’s SLRIs. Tables 2 and 4 show that target clouds with larger masses than the standard cloud are also more likely to achieve collapse and significant injection. Table 5 shows that the maximum temperatures assumed for the shock and post-shock gas can also have an effect on the outcome.

Table 1 shows that more post-shock wind is likely to be accreted by the collapsing protostar than shock wave matter, by as much as a factor of 10. This is similar to the result found in the 2D models of Boss & Foster (1998). Hence, these models suggest that explaining the evidence for low $^{60}\text{Fe}/^{56}\text{Fe}$ ratios and high $^{26}\text{Al}/^{27}\text{Al}$ ratios as being due to their synthesis in different layers of a massive star (Tang & Dauphas 2012) will only work if the inner layers fall back onto the stellar remnant, not if they are ejected and follow behind the leading edge of the SN shock.

Finally, we note that the present estimates strictly apply only to the injection of shock wave gas carrying SLRIs, or dust grains small enough to be carried along with the gas. Large grains can be injected with higher efficiencies, as found by Ouellette et al. (2010). However, such large grains appear to be rare in the ISM, and Boss & Keiser (2010) concluded that the overall effect should not be large. Nevertheless, to the extent that large grains carrying SLRIs are present in shock waves, the present estimates of SLRI injection efficiencies should be considered to be lower bounds.

4. Conclusions

We have shown that achieving simultaneous triggered collapse of a dense molecular cloud core and injection of significant shock wave material is by no means an easy task to achieve, at least not if the shock-cloud interaction is required to inject sufficient SLRIs to match the inferred abundances for the Solar System’s most primitive meteoritical components. Nevertheless, SN shock waves remain as the most likely stellar source of shock-injected SLRIs, though AGB stars remain in the running, provided that the enhanced injection efficiencies found for rotating target cloud cores can raise the dilution factors to the required levels. AGB stars have a significant probability of passing through a molecular cloud complex (Kastner & Myers 1994), and our models show that their winds can trigger cloud core collapse, so an AGB star source cannot be discounted on these grounds. Wolf-Rayet star winds, on the other hand, do not appear to be suitable sources of the shock waves considered in this work, as their hot, fully ionized winds are driven by thermal pressure, as opposed to the momentum-driven, relatively cool winds shown here to be capable of triggering collapse and injection. When collapse does occur, significant post-shock wind gas and dust is likely to be accreted by the growing protostar, adding to the isotopic brew obtained from the stellar source of the shock wave.

Future fully 3D models of this triggering and injection scenario (e.g., Boss & Keiser 2012) need to consider the case of rotating target clouds, in order to boost the injection efficiencies and give this scenario the best possible chance of remaining as a contender for explaining the origin of the Solar System’s SLRIs. Such models are currently in progress at DTM.

We thank Roger Chevalier for discussions long ago, and the referee for suggesting several improvements to the manuscript. The calculations were performed on the dc101 cluster at DTM. This research was supported in part by NASA Origins of Solar Systems grant NNX09AF62G and is contributed in part to NASA Astrobiology Institute grant NNA09DA81A. The software used in this work was in part developed by the DOE-supported ASC/Alliances Center for Astrophysical Thermonuclear Flashes at the University of Chicago.

REFERENCES

- Anders, E., & Grevesse, N. 1989, *Geochim. Cosmochim. Acta*, 53, 197
Blair, W. P., Sankrit, R., Raymond, J. C., & Long, K. S. 1999, *AJ*, 118, 942
Boss, A. P. 2012, *Annu. Rev. Earth Planet. Sci.*, 40, 23

- Boss, A. P., & Foster, P. N. 1998, *ApJ*, 494, L103
- Boss, A. P., & Keiser, S. A. 2010, *ApJL*, 717, L1
- Boss, A. P., & Keiser, S. A. 2012, *ApJL*, 756, L9
- Boss, A. P., et al. 2008, *ApJ*, 686, L119
- Boss, A. P., et al. 2010, *ApJ*, 708, 1268
- Burkert, A., & Alves, J. 2009, *ApJ*, 695, 1308
- Dauphas, N., & Chaussidon, M. 2011, *Annu. Rev. Earth Planet. Sci.*, 39, 351
- Diehl, R., et al. 2010, *A&A*, 522, A51
- Dukes, D., & Krumholz, M. R. 2012, *ApJ*, 754, 56
- Foster, P. N., & Boss, A. P. 1996, *ApJ*, 468, 784
- Fryxell, B., Olson, K., Ricker, P., et al. 2000, *ApJS*, 131, 273
- Gaidos, E., Krot, A. N., Williams, J. P., & Raymond, S. N. 2009, *ApJ*, 696, 1854
- Goodman, A. A., Benson, P. J., Fuller, G. A., & Myers, P. C. 1993, *ApJ*, 406, 528
- Gounelle, M., & Meynet, G. 2012, *A&A*, 545, A4
- Gritschneider, M., Lin, D. N. C., Murray, S. D., et al. 2012, *ApJ*, 745, 22
- Huss, G. R., Meyer, B. R., Srinivasan, G., Goswami, J. N., & Sahijpal, S. 2009, *Geochim. Cosmochim. Acta*, 73, 4922
- Jacoby, G. H., Ferland, G. J., & Korista, K. T. 2001, *ApJ*, 560, 272
- Kastner, J. H., & Myers, P. C. 1994, *ApJ*, 421, 605
- Krot, A. N., Makide, K., Nagashima, K., et al. 2012, *Meteorit. Planet. Sci.*, 47, 1948
- Liu, M.-C., Chaussidon, M., Srinivasan, G., & McKeegan, K. D. 2012, *ApJ*, 761, 137
- Lugaro, M., Doherty, C. L., Karakas, A. I., et al. 2012, *Meteorit. Planet. Sci.*, 47, 1998
- MacPherson, G. J., Kita, N. T., Ushikubo, T., Bullock, E. S., & Davis, A. M. 2012, *Earth Planet. Sci. Lett.*, 331-332, 43
- Moynier, F., Blichert-Toft, J., Wang, K., Herzog, G. F., & Albarede, F. 2011, *ApJ*, 741, 71
- Neufeld, D. A., & Kaufman, M. J. 1993, *ApJ*, 418, 263
- Ouellette, N., Desch, S. J., & Hester, J. J. 2007, *ApJ*, 662, 1268
- Ouellette, N., Desch, S. J., & Hester, J. J. 2010, *ApJ*, 711, 597
- Pan, L., Desch, S. J., Scannapieco, E., & Timmes, F. X. 2012, *ApJ*, 756, 102

- Pierce, M. J., Frew, D. J., Parker, Q. A., & Köppen, J. 2004, *Publ. Astron. Soc. Australia*, 21, 334
- Reach, W. T., Rho, J., & Jarrett, T. H. 2005, *ApJ*, 618, 297
- Ruoskanen, J., et al. 2011, *A&A*, 534, A122
- Schnee, S., et al. 2010, *ApJ*, 718, 306
- Takigawa, A., et al. 2008, *ApJ*, 688, 1382
- Tang, H., & Dauphas, N. 2012, *Earth Planet. Sci. Lett.*, 359-360, 248
- Tatischeff, V., Duprat, J., & De Séreville, N. 2010, *ApJL*, 714, L26
- Telus, M., Huss, G. R., Oglione, R. C., Nagashima, K., & Tachibana, S. 2012, *Meteorit. Planet. Sci.*, 47, 2013
- Trigo-Rodríguez, J. M., et al. 2009, *Meteorit. & Planet. Sci.*, 44, 627
- Tur, C., Heger, A., & Austin, S. M. 2010, *ApJ*, 718, 357
- van Marle, A. J., & Keppens, R. 2012, *A&A*, 547, A3.
- Walter, F. M., Alcalá, J. M., Neuhäuser, R., Sterzik, M., & Wolk, S. J. 2000, in *Protostars & Planets IV*, ed. V. Mannings, A. P. Boss, & S. S. Russell (Tucson, AZ: Univ. Arizona Press), 273
- Williams, J. P., Blitz, L., & McKee, C. F. 2000, in *Protostars & Planets IV*, ed. V. Mannings, A. P. Boss, & S. S. Russell (Tucson, AZ: Univ. Arizona Press), 97

Table 1. Results for the three standard $2.2 M_{\odot}$ target cloud models with varied shock speeds (v_s in km s^{-1}), showing the amount of mass in the collapsing protostar derived from the shock wave (M_s), post-shock wind (M_{psw}), and ambient medium (M_{am}), along with the injection efficiency (f_i) for the shock wave material.

Model	v_s	M_s/M_{\odot}	M_{psw}/M_{\odot}	M_{am}/M_{\odot}	f_i
v10	10	8.0×10^{-5}	1.5×10^{-4}	2.0×10^{-6}	4.7×10^{-3}
v40	40	1.5×10^{-4}	1.1×10^{-3}	4.0×10^{-6}	8.8×10^{-3}
v70	70	5.5×10^{-4}	4.6×10^{-3}	3.7×10^{-5}	3.2×10^{-2}

Table 2. Results for the $5.4 M_{\odot}$ target cloud models with varied shock gas densities (in units of the standard shock density, $\rho_s = 3.6 \times 10^{-20} \text{ g cm}^{-3}$) and shock widths (in units of the standard shock width, $w_s = 0.0030 \text{ pc}$) at the standard shock speed of $v_s = 40 \text{ km s}^{-1}$. N_y is the number of blocks in the grid in the $y = Z$ direction. M_s is the amount of mass in the collapsing protostar derived from the shock wave and f_i is the injection efficiency for the shock wave material.

Model	N_y	w_s	ρ_s	M_s/M_{\odot}	f_i
v40-m5.4-r2	20	1	1	4.5×10^{-6}	6.4×10^{-5}
v40-m5.4-r2-w0.1-s250	30	0.1	250	3.0×10^{-3}	1.7×10^{-3}
v40-m5.4-r2-w0.1-s300	30	0.1	300	1.3×10^{-3}	6.2×10^{-4}
v40-m5.4-r2-w0.1-s400	30	0.1	400	0	0

Table 3. Results for the $2.2 M_{\odot}$ target cloud models with varied initial rotation rates (Ω_i , in rad s^{-1}) about the $Z = y$ axis, compared to the standard, non-rotating model v40. All models had $v_s = 40 \text{ km s}^{-1}$. M_s is the amount of mass in the collapsing protostar derived from the shock wave and f_i is the injection efficiency for the shock wave material.

Model	Ω_i	M_s/M_{\odot}	f_i
v40	0.0	1.5×10^{-4}	8.8×10^{-3}
v40-o16	10^{-16}	4.7×10^{-4}	2.8×10^{-3}
v40-o15	10^{-15}	8.4×10^{-4}	4.9×10^{-2}
v40-o14.5	$10^{-14.5}$	1.0×10^{-3}	5.9×10^{-2}
v40-o14	10^{-14}	1.0×10^{-3}	5.9×10^{-2}
v40-o13.5	$10^{-13.5}$	1.3×10^{-3}	7.6×10^{-2}
v40-o13	10^{-13}	1.0×10^{-3}	5.9×10^{-2}
v40-o12.5	$10^{-12.5}$	7.8×10^{-4}	4.6×10^{-2}
v40-o12	10^{-12}	0	0

Table 4. Results for the $1.0 M_{\odot}$ target cloud models with varied shock speeds (v_s in km s^{-1}), showing the amount of mass in the collapsing protostar derived from the shock wave (M_s) and the injection efficiency (f_i) for the shock wave material.

Model	v_s	M_s/M_{\odot}	f_i
v5-m1.0	5	9.3×10^{-5}	2.8×10^{-3}
v10-m1.0	10	1.7×10^{-3}	5.2×10^{-2}
v15-m1.0	15	4.6×10^{-5}	1.4×10^{-3}
v20-m1.0	20	0	0
v40-m1.0	40	0	0
v70-m1.0	70	0	0

Table 5. Results for the $2.2 M_{\odot}$ target cloud models with varied shock (T_s in K) and post-shock wind (T_{ps} in K) temperatures and varied shock gas densities (in units of the standard shock density, $\rho_s = 3.6 \times 10^{-20}$ g cm $^{-3}$), all for the standard shock speed of $v_s = 40$ km s $^{-1}$. M_s is the amount of mass in the collapsing protostar derived from the shock wave and f_i is the injection efficiency.

Model	T_s	T_{ps}	ρ_s	M_s/M_{\odot}	f_i
v40	1000	1000	1	1.5×10^{-4}	8.8×10^{-3}
v40-T500	500	500	1	1.8×10^{-4}	9.2×10^{-3}
v40-T100	100	100	1	5.2×10^{-6}	2.7×10^{-4}
v40-T100-s10	100	100	10	3.5×10^{-3}	1.8×10^{-2}
v40-T100-s100	100	100	100	0	0

Table 6. Results for the $2.2 M_{\odot}$ target cloud models with varied shock gas densities (in units of the standard shock density, $\rho_s = 3.6 \times 10^{-20}$ g cm $^{-3}$) and shock widths (in units of the standard shock width, $w_s = 0.0030$ pc) at a shock speed of $v_s = 10$ km s $^{-1}$.

Model	N_y	w_s	ρ_s	M_s/M_{\odot}	f_i
v10	15	1	1	8.0×10^{-5}	4.7×10^{-3}
v10-s0.1	15	1	0.1	1.1×10^{-4}	6.5×10^{-2}
v10-s10-30	30	1	10	9.7×10^{-4}	5.7×10^{-3}
v10-s100-40	40	1	100	0.0	0.0
v10-w0.1	15	0.1	1	5.2×10^{-5}	7.4×10^{-2}
v10-w0.1-s10	15	0.1	10	4.8×10^{-4}	6.9×10^{-2}
v10-w0.1-s100-30	30	0.1	100	2.2×10^{-3}	3.1×10^{-2}
v10-w0.1-s200-30	30	0.1	200	6.7×10^{-3}	4.8×10^{-2}
v10-w0.1-s300-30	30	0.1	300	7.5×10^{-3}	3.4×10^{-2}
v10-w0.1-s400-30	30	0.1	400	1.9×10^{-2}	6.8×10^{-2}
v10-w0.1-s600-30	30	0.1	600	6.5×10^{-3}	1.5×10^{-2}
v10-w0.1-s800-30	30	0.1	800	2.9×10^{-2}	4.9×10^{-2}
v10-w0.1-s1000-30	30	0.1	1000	4.6×10^{-2}	6.3×10^{-2}
v10-w0.1-s2000-30	30	0.1	2000	6.3×10^{-3}	4.3×10^{-3}
v10-w0.1-s4000-30	30	0.1	4000	1.3×10^{-2}	4.5×10^{-3}
v10-w10-s10-30	30	10	10	0.0	0.0
v10-w10-s30-30	30	10	30	0.0	0.0
v10-w10-s50-30	30	10	50	0.0	0.0
v10-w10-s100-30	30	10	100	1.0×10^0	5.0×10^{-2}

Table 7. Results for the $2.2 M_{\odot}$ target cloud models with varied shock gas densities (in units of the standard shock density, $\rho_s = 3.6 \times 10^{-20} \text{ g cm}^{-3}$) and shock widths (in units of the standard shock width, $w_s = 0.0030 \text{ pc}$) at a shock speed of $v_s = 40 \text{ km s}^{-1}$. Injection efficiencies estimated with a different methodology by Boss & Keiser (2010) are listed in the last column.

Model	N_y	w_s	ρ_s	M_s/M_{\odot}	f_i	f_i (BK2010)
v40	15	1	1	1.5×10^{-4}	8.8×10^{-3}	1×10^{-3}
v40-s0.1	15	1	0.1	5.3×10^{-5}	3.1×10^{-2}	6×10^{-5}
v40-s10	15	1	10	6.4×10^{-4}	3.8×10^{-3}	3×10^{-3}
v40-s100-30	30	1	100	0.0	0.0	0.0
v40-w0.1	15	0.1	1	3.5×10^{-5}	5.0×10^{-2}	2×10^{-4}
v40-w0.1-s10	15	0.1	10	4.8×10^{-4}	6.9×10^{-2}	2×10^{-3}
v40-w0.1-s100	15	0.1	100	2.5×10^{-3}	3.6×10^{-2}	1×10^{-2}
v40-w0.1-s200	15	0.1	200	3.9×10^{-3}	2.8×10^{-2}	2×10^{-2}
v40-w0.1-s400-20	20	0.1	400	6.5×10^{-4}	2.3×10^{-3}	4×10^{-2}
v40-w0.1-s800-20	20	0.1	800	0.0	0.0	0.0
v40-w10	15	10	1	4.2×10^{-4}	2.2×10^{-3}	4×10^{-4}
v40-w10-s10	15	10	10	0.0	0.0	0.0

Table 8. Results for the $2.2 M_{\odot}$ target cloud models with varied shock gas densities (in units of the standard shock density, $\rho_s = 3.6 \times 10^{-20} \text{ g cm}^{-3}$) and shock widths (in units of the standard shock width, $w_s = 0.0030 \text{ pc}$) at a shock speed of $v_s = 70 \text{ km s}^{-1}$.

Model	N_y	w_s	ρ_s	M_s/M_{\odot}	f_i
v70	15	1	1	5.5×10^{-4}	3.2×10^{-2}
v70-s0.1	15	1	0.1	1.7×10^{-5}	1.0×10^{-2}
v70-s10	15	1	10	0.0	0.0
v70-s100-30	30	1	100	0.0	0.0
v70-w0.1	15	0.1	1	6.0×10^{-6}	8.6×10^{-3}
v70-w0.1-s10	15	0.1	10	6.8×10^{-6}	8.9×10^{-4}
v70-w0.1-s100	15	0.1	100	3.9×10^{-4}	5.6×10^{-3}
v70-w0.1-s200	15	0.1	200	0.0	0.0
v70-w0.1-s200-20	20	0.1	200	0.0	0.0
v70-w0.1-s400-20	20	0.1	400	0.0	0.0
v70-w10	15	10	1	5.8×10^{-4}	3.1×10^{-3}
v70-w10-s10	15	10	10	0.0	0.0

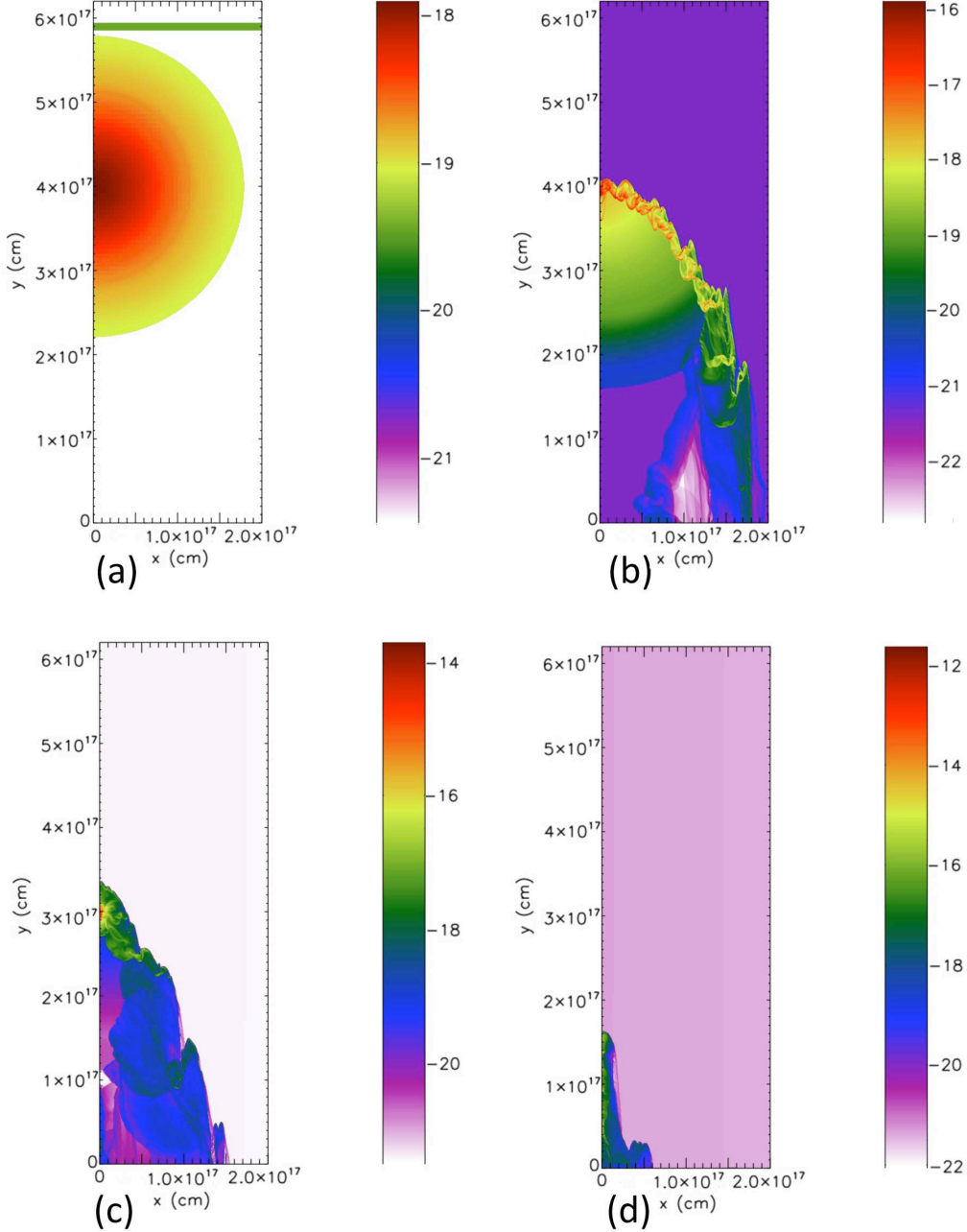


Fig. 1.— Time evolution of model v40, showing the log of the density distribution at four times: a) 0.0 yr, b) 3.34×10^4 yr, c) 6.58×10^4 yr, and d) 10.4×10^4 yr. The initial (a) shock wave (green) moves downward at 40 km s^{-1} to strike and compress the target cloud, generating Rayleigh-Taylor fingers (b), leading to the onset of dynamic collapse (c-d) and the formation of a protostar. The 2D AMR code symmetry axis is along the left hand side of the plot. The $R = x$ axis is horizontal and the $Z = y$ axis is vertical.

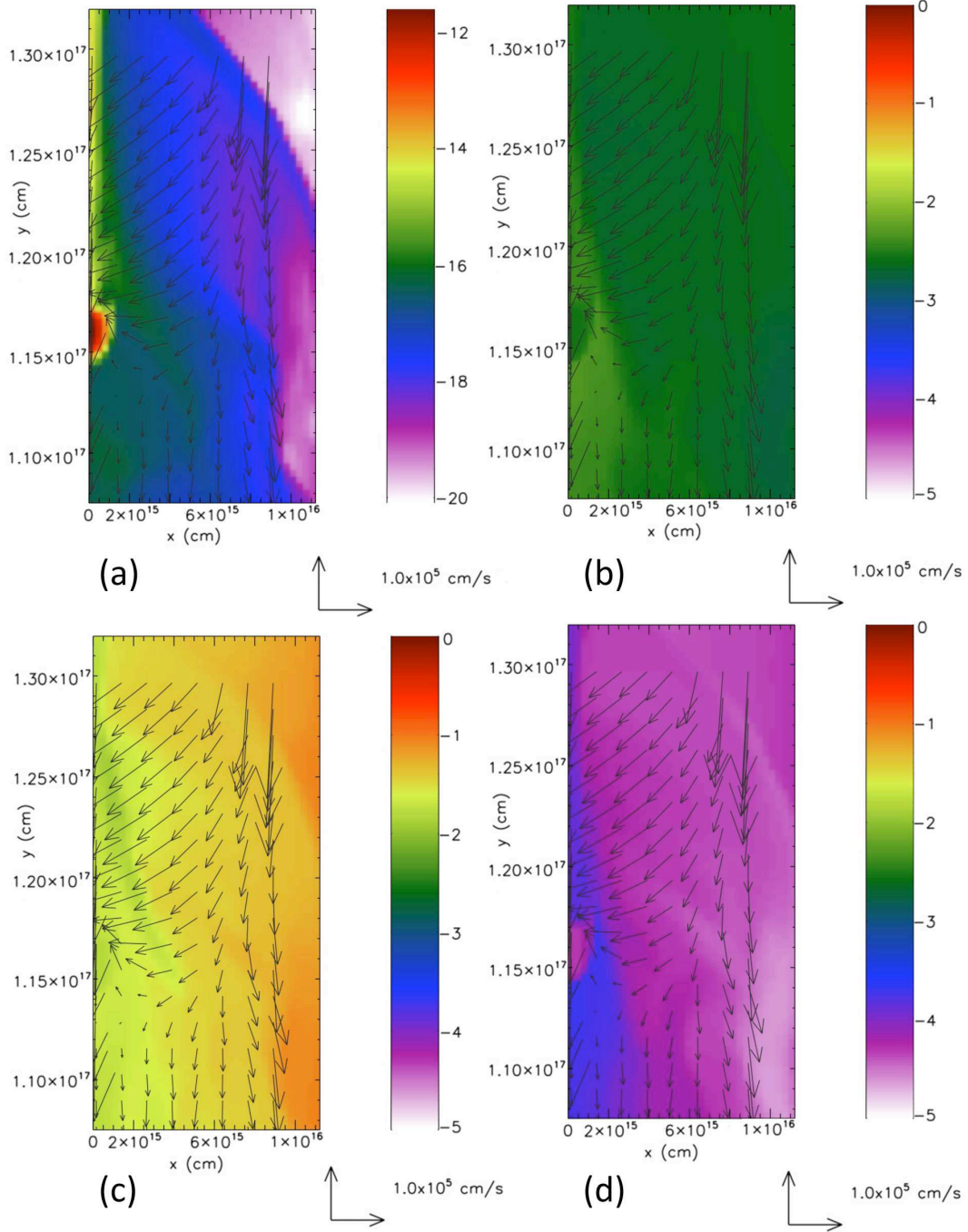


Fig. 2.— Model v40 after 10.4×10^4 yr, plotted in the same manner as in Figure 1, for four fields: a) log of the total gas density, b) log shock wave gas density, c) log post-shock wind gas density, and d) log ambient medium gas density. Velocity vectors are plotted for every fourth grid point in each direction, with the scale bar denoting 1 km s^{-1} .

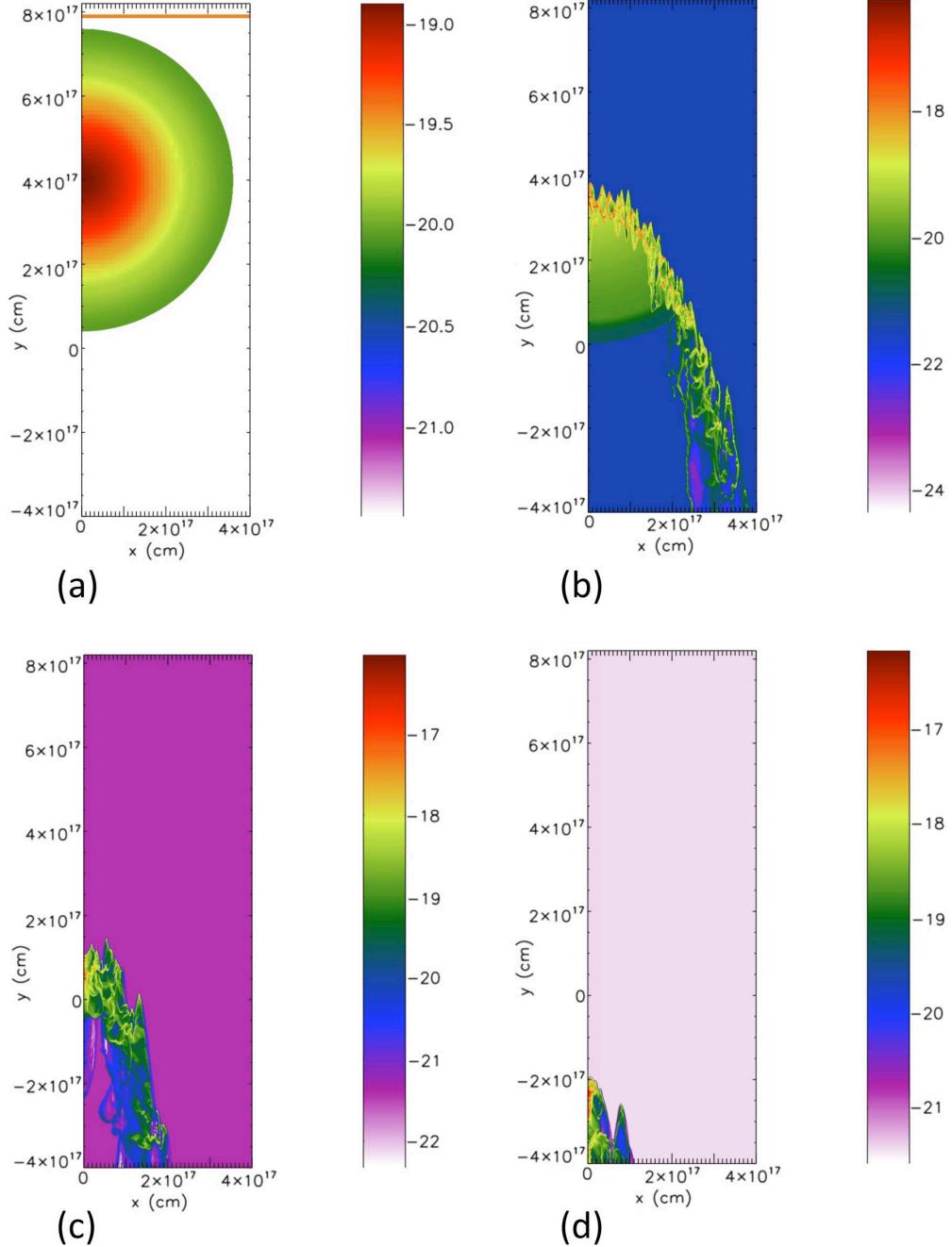


Fig. 3.— Time evolution of model v40-m1.9-r2, plotted as in Figure 1, at times: a) 0.0 yr, b) 3.00×10^4 yr, c) 6.00×10^4 yr, and d) 8.99×10^4 yr. With a target cloud density 10 times lower than for model v40 (Figures 1 and 2) and a cloud radius twice as large, the same standard 40 km s^{-1} shock smacks the cloud b) and shreds it c), without inducing sustained gravitational collapse. The maximum density reached never exceeds $\sim 10^{-16} \text{ g cm}^{-3}$.

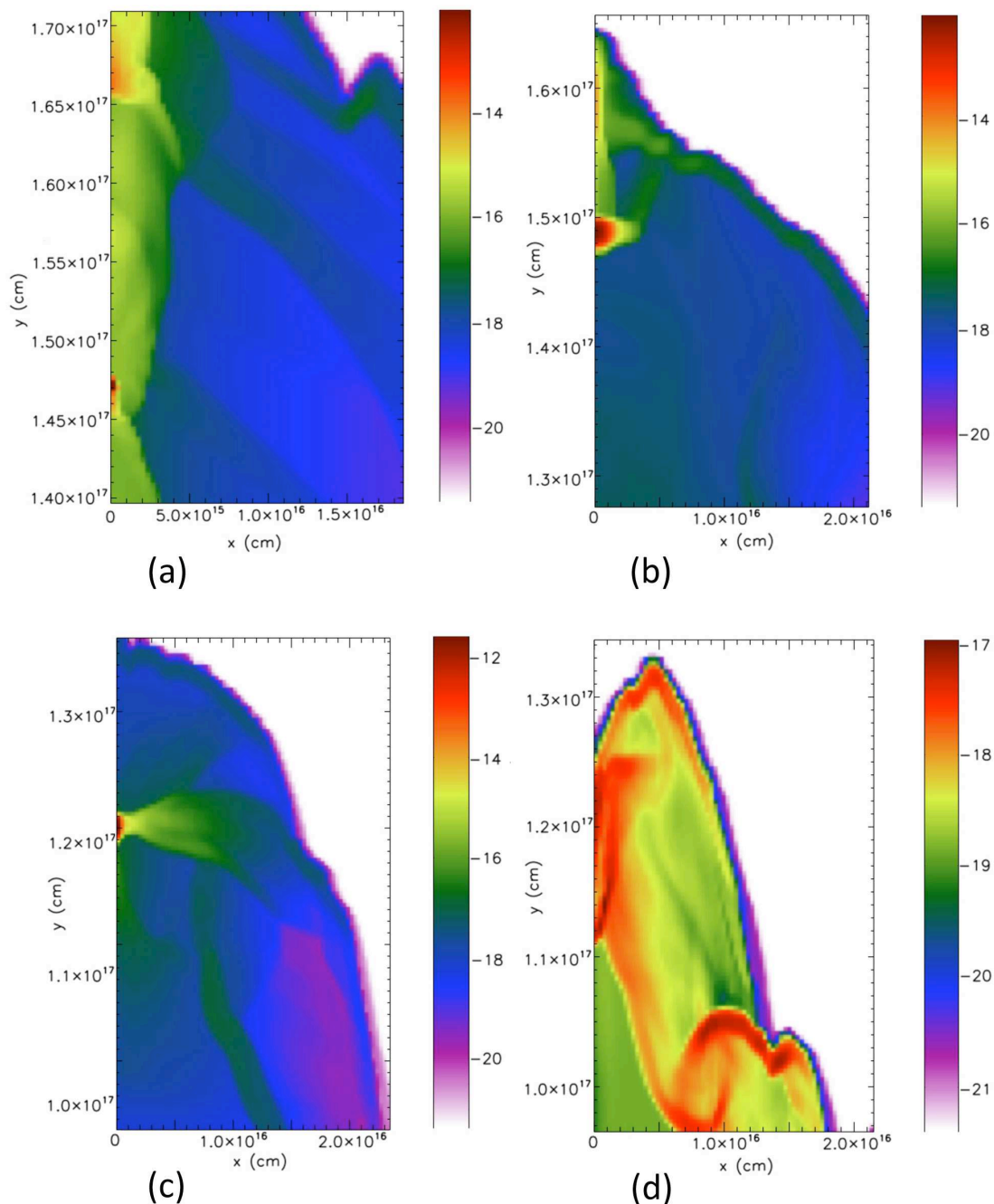


Fig. 4.— Results of models with progressively larger initial cloud rotation rates about the $Z = y$ axis, showing the log of the gas density, plotted as in Figure 1: a) model v40-o15 at 1.00×10^5 yr, b) model v40-o14 at 1.05×10^5 yr, c) model v40-o13 at 1.10×10^5 yr, and d) model v40-o12 at 8.99×10^4 yr. Model v40-o13 collapses and forms an extended protostellar disk, while model v40-o12 is so distended by the rotation that it fails to form a protostar, and is shredded instead.

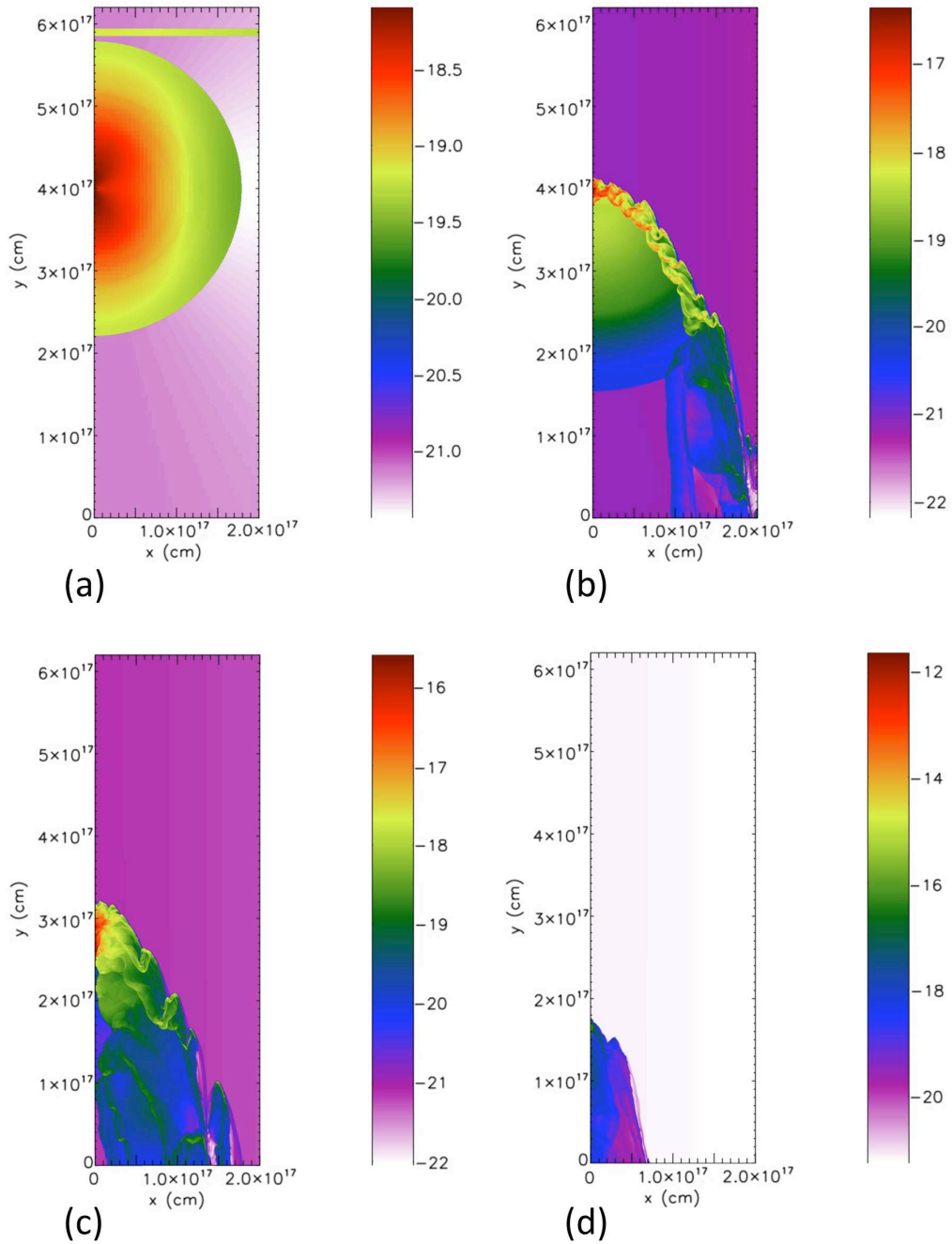


Fig. 5.— Time evolution of model v15-m1.0, showing the log of the density distribution at four times: a) 0.0 yr, b) 4.47×10^4 yr, c) 9.02×10^4 yr, and d) 14.0×10^4 yr, plotted as in Figure 1.